Electronic Supplementary Material

$Ni_{1-x}M_xSe_2$ (M = Fe, Co, Cu) nanowires as anodes for ammonia-borane electrooxidation and the derived ultrathin $Ni_{1-x}M_xSe_{2-y}$−OOH nanosheets as efficient electrocatalysts for oxygen evolution

Guojing Wang, Hu Wang, Tao Chen, and Yiwei Tan*

State Key Laboratory of Materials-Oriented Chemical Engineering, School of Chemistry and Chemical Engineering, Nanjing Tech University, Nanjing 211816, China, Email: ytan@njtech.edu.cn, Tel: +86-25-83172267

Experimental Section

Materials. Nickel(II) chloride hexahydrate ($NiCl_2·6H_2O$, 99%), nickel(II) nitrate hexahydrate ($Ni(NO_3)_2·6H_2O$, 98%), copper(II) chloride dihydrate ($CuCl_2·2H_2O$, 99%), cobalt(II) nitrate hexahydrate ($Co(NO_3)_2·6H_2O$, ≥98%), iron(III) chloride (anhydrous, $FeCl_3$, 98%), urea (NH_2CONH_2, 99%), ammonia-borane (NH_3BH_3, 97%), nitric acid (HNO_3, 68–70%), sodium borohydride ($NaBH_4$, 98%), sodium sulfate (anhydrous, Na_2SO_4, 99%), and diethylene glycol ($(HOCH_2CH_2)_2O$, 99%) were commercially available from Sinopharm Chemical Reagent Co., Ltd.. Selenium powder (99.5%, 325 mesh) and *N*-methyl-2-pyrrolidinone (NMPD, 99%) were purchased from Alfa Aesar. Carbon fiber paper (CFP, ~180 μm in thickness) was purchased from Wuhan Cetech Co., Ltd.. All reagents were used without any further purification. Ultrapure water (18.2 MΩ) produced with a Milli-Q purification system was used in the synthesis and electrochemical measurements. CFP was thoroughly washed by sonication in acetone and than in water alternatively for 3 times and then pretreated with concentrated nitric acid (68–70%) at the 75 °C for 90 min to achieve the surface hydroxylation of CFP. After being washed with water, the pretreated CFP was used as the support for the syntheses of various integrated catalysts.

Characterization of materials

Scanning electron microscopy (SEM) images and surface elemental mapping data were acquired using a Hitachi S-4800 field-emission scanning electron microscope equipped with an energy-dispersive X-ray (EDX) spectroscopy detector (Oxford) to investigate the morphology and surface chemical composition of the catalysts, operating at an acceleration voltage of 5 and 20 kV, respectively. Transmission electron microscopy (TEM) images were obtained using an FEI Tecnai G2 Spirit Bio TWIN transmission electron microscope operated at an accelerating voltage of 100 kV. High-resolution TEM (HRTEM) and scanning TEM (STEM) micrographs, and EDX (or EELS) elemental maps were acquired using an FEI Tecnai G2 F20 S-TWIN transmission electron microscope operated at 200 kV and an FEI ETEM Titan G2 60-300 Cs-corrected scanning transmission electron microscope equipped with a spherical aberration corrector for the electron beam and a Gatan Image Filter (GIF-Quantum) for electron energy loss spectroscopy (EELS) analysis operated at 300 kV to probe the crystallographic structure and composition of samples. STEM micrographs and EDX elemental maps were obtained in high-angle annular dark field (HAADF) mode to provide the bulk chemical composition of samples. The specimens for TEM observations were scratched from the CFP support and sonicated before dropping them onto 300 mesh carbon-coated copper or molybdenum grids. Atomic force microscopy (AFM) measurements were implemented by Vecco Dimension 3100 SPM system. To analyze the surface composition and elemental oxidation states of samples, X-ray photoelectron spectroscopy (XPS) measurements were carried out using a PHI5000 VersaProbe (ULVAC-PHI) spectrometer with a hemispherical energy analyzer, employing a monochromatized microfocused Al-Kα (hv = 1486.58 eV) X-ray source. Samples for XPS measurements were carefully scratched from the CFP support and then sputtered by repeated cycles of Ar^+ ions to obtain clean sample surfaces. The binding energies (BEs) of the core levels were calibrated by setting the adventitious C 1s peak at 284.8 eV. Survey spectra of the samples in the BE range of 0–1000 eV and the core level spectra of the elemental signals were collected with a step size of 1 and 0.125 eV, respectively. To obtain the phase and structure of samples, the X-ray diffraction (XRD) patterns were recorded

using a Rigaku SmartLab diffractometer with a Cu Kα X-ray source (λ = 1.5406 Å, generated at 40 kV and 100 mA) at a scanning rate of 0.06° s^{-1}, and scanned in the Bragg–Brentano mode from 2θ of 10° to 90° in 0.02° increments. The CFP coated with an active material was directly used as the specimen for XRD characterization after cleaning treatment. The chemical composition of the catalyst was determined by EDX quantitative analysis and inductively coupled plasma atomic emission spectrometry (ICP-AES, Prodigy, Leeman Labs Inc., λ = 165–800 nm, As = 200 nm) measurements after dissolving the sample in aqua regia. Raman spectra were collected by using a Jobin-Yvon LabRAM HR800 Raman spectrometer (excitation wavelength: 532 nm).

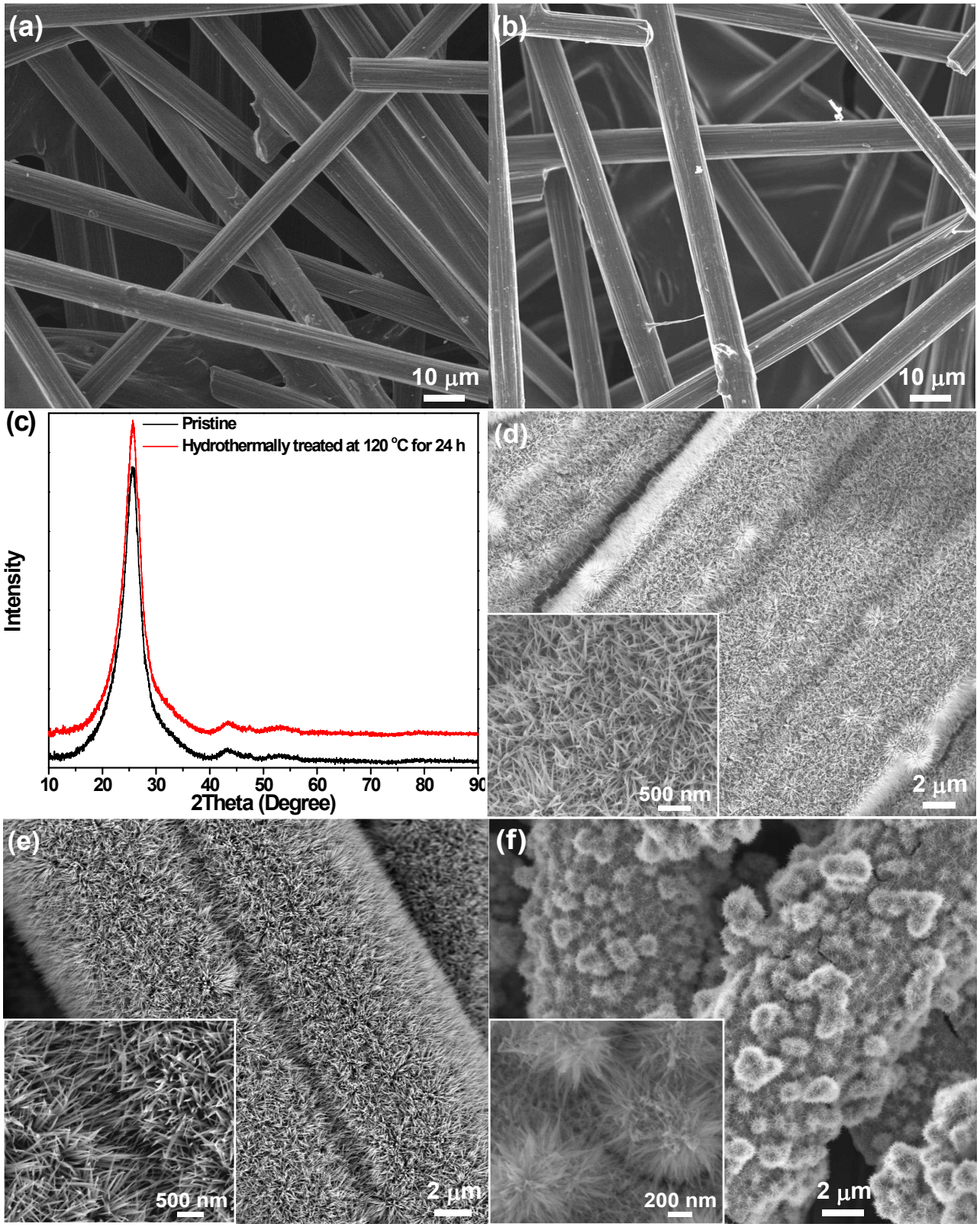

Figure S1. SEM micrographs of (a) the pristine and (b) hydrothermally treated CFP supports. (c) The corresponding XRD patterns. Hydrothermal treatment of CFP supports was carried out at 120 ºC for 24 h. SEM micrographs of (d) Ni–Cu basic carbonate, (e) Ni–Co basic carbonate, and (f) Ni–Fe basic carbonate precursors. The insets in panel (d–f) show the corresponding enlarged SEM images to clearly demonstrate the dense arrays of Ni–M basic carbonate precursor NWs. Various Ni–M basic carbonate precursors were formed based on the following reaction equation:

$$2(1-x)Ni^{2+} + 2xM^{2+} + 2NH_2CONH_2 + 5H_2O = \{Ni_{1-x}M_x\}_2(OH)_2CO_3 + 4NH_4^+ + CO_2 \qquad (S1)$$

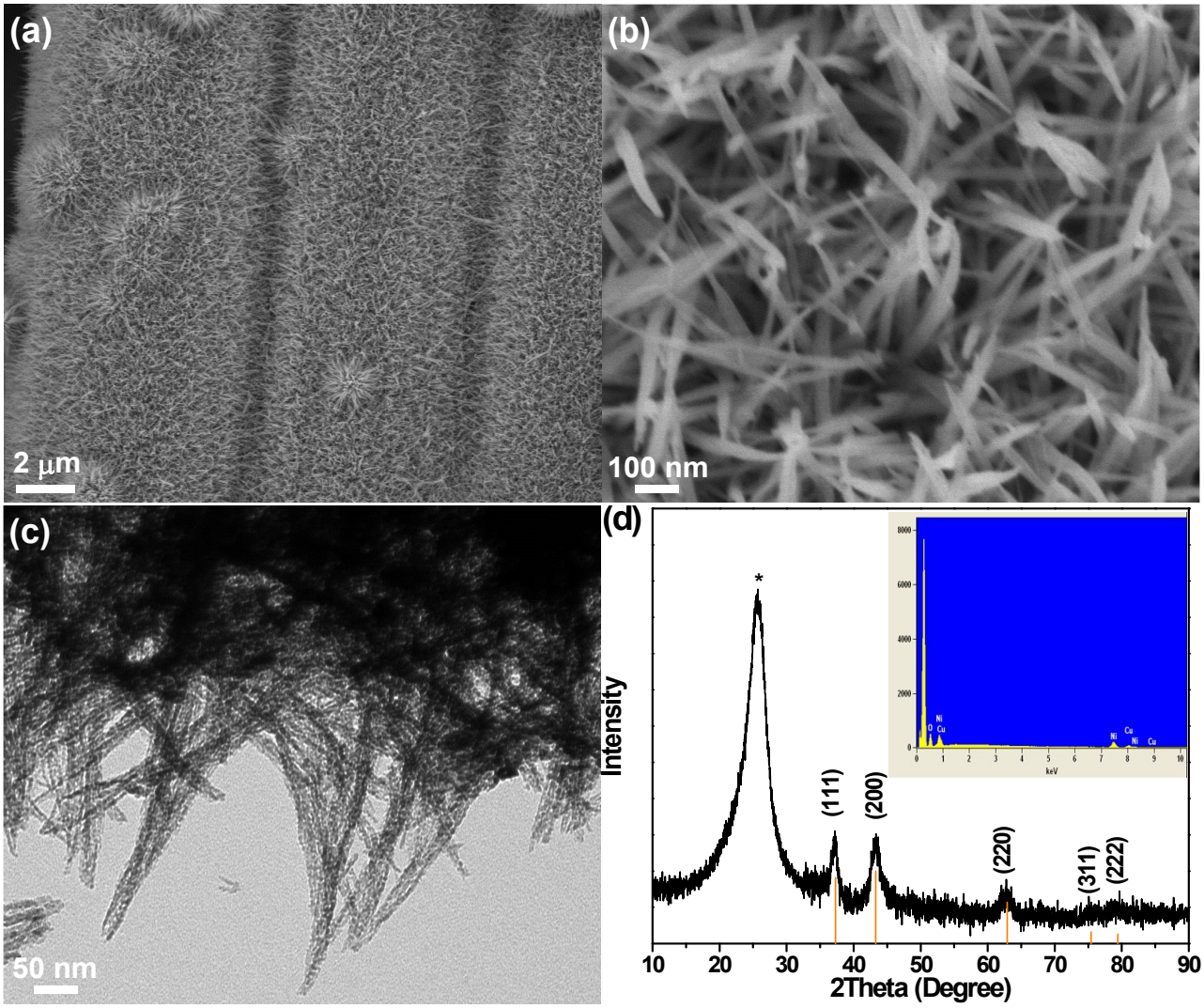

Figure S2. Morphological and structural characterization of the $Ni_{1-x}Cu_xO$/CFP. (a) Low- and (b) high-magnification SEM micrographs, (c) TEM image, and (d) XRD pattern. For comparison, the intensities and positions for the NiO reference are given according to the JCPDF database (JCPDF No. 04-0835, orange lines at the bottom of panel (d)).

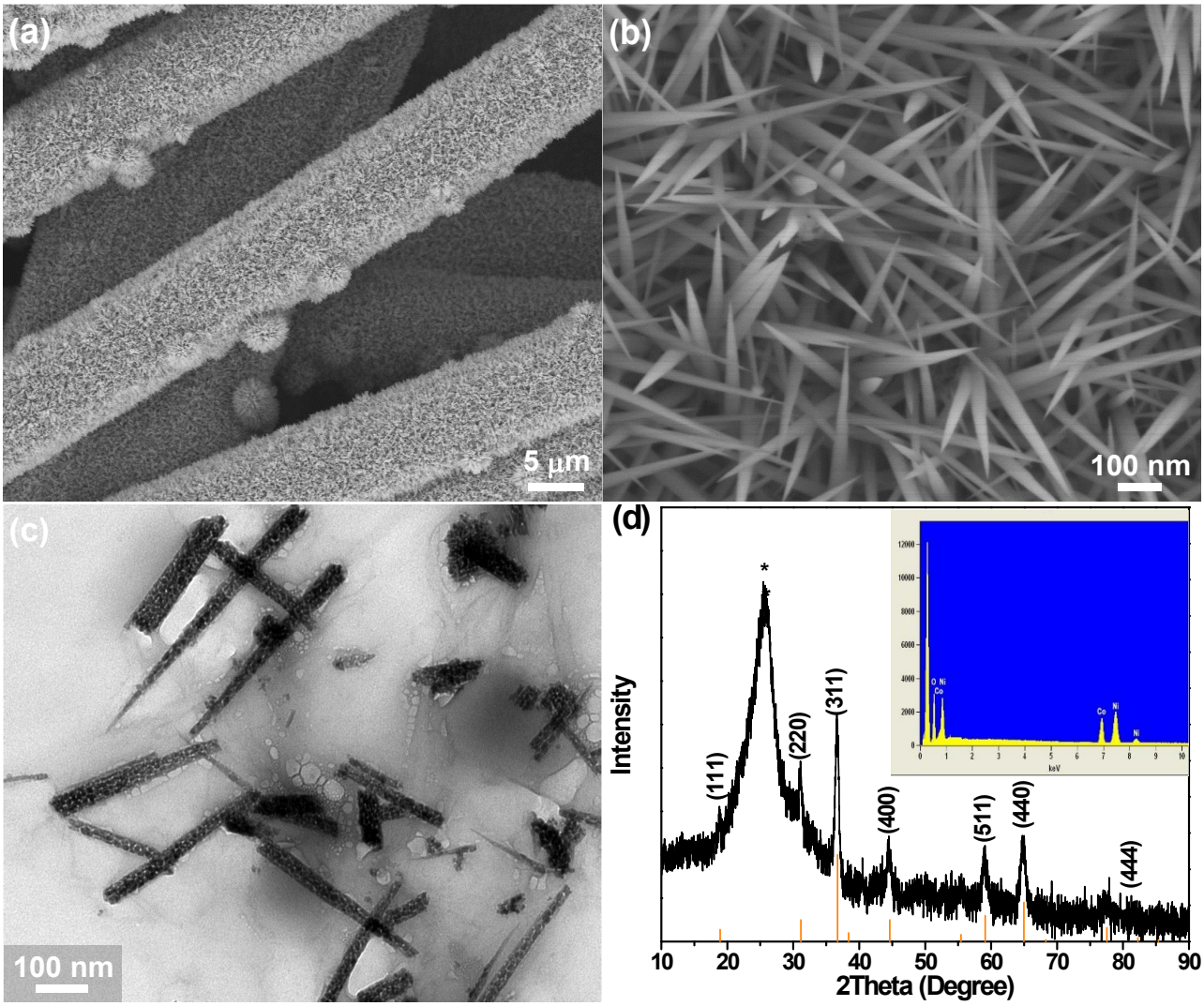

Figure S3. Morphological and structural characterization of the $NiCo_2O_4$/CFP. (a) Low- and (b) high-magnification SEM micrographs, (c) TEM image, and (d) XRD pattern. For comparison, the intensities and positions for the $NiCo_2O_4$ reference are given according to the JCPDF database (JCPDF No. 20-0781, orange lines at the bottom of panel (d)).

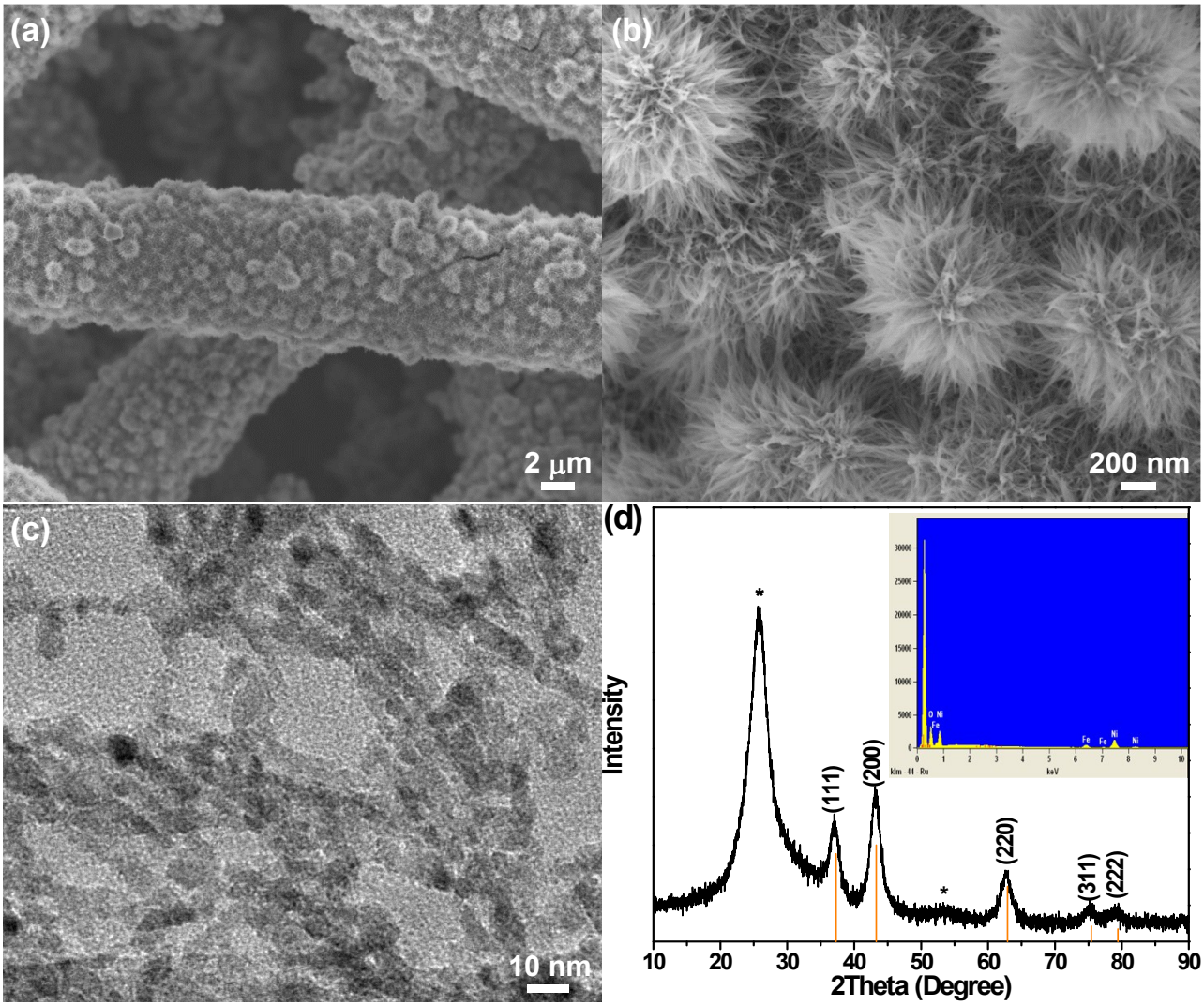

Figure S4. Morphological and structural characterization of the $Ni_{1-x}Fe_xO$/CFP. (a) Low- and (b) high-magnification SEM micrographs, (c) TEM image, and (d) XRD pattern. For comparison, the intensities and positions for the NiO reference are given according to the JCPDF database (JCPDF No. 04-0835, orange lines at the bottom of panel (d)).

The nickel-based bimetallic oxide NW precursors grown on CFP were prepared by heat-treating the Ni−M (M = Cu, Co, Fe) basic carbonate precursor. In contrast to the pristine CFP with smooth surface (Figure S1), the low-magnification SEM images in Figure S2a, S3a, and S4a unambiguously illustrate that the entire surface of CFP is homogeneously coated with nanostructured nickel-based bimetallic oxides after annealing treatment in air. The enlarged SEM images in Figure S2b, S3b, and S4b show that dense oxide NW arrays on CFP are achieved and the NWs of each sample have a highly uniform size distribution. Intriguingly, a large number of Ni−Fe oxide NWs in radial pattern self-organize into numerous flower-like spherical superstructures (Figure S4b). Analysis through the combination of SEM and TEM images reveals that the Ni−Cu and Ni−Co oxide NWs usually terminate with a sharp tip, form a sharp needle-like morphology, and have a length and width in the range of 500−1000 and 15−50 nm, respectively (also see Figure S2c and S3c). In particular, the dissociation of the −OH and $-CO_3^{2-}$ groups in the precursor during annealing leads to the pronounced porous features for Ni−M oxide NWs (Figure S2c, S3c, and S4c). However, the Ni−Fe oxide NWs with a diameter of 5−8 nm are much thinner than the Ni−Cu and Ni−Co oxide NWs (Figure S4c). To determine the crystalline structure, XRD diffractograms are depicted in Figure S2d, S3d, and S4d. By indexing these XRD diffractograms using ICDD PDF cards, it is found that the as-prepared Ni−Cu and Ni−Fe oxide NWs possess a highly crystalline face-centered cubic NiO phase with the $Fm\bar{3}m$ space group, while the Ni−Co oxide NWs are of characteristic cubic $NiCo_2O_4$ structure with the $Fd3m$ space group. No diffraction peaks from copper oxides, cobalt oxides, or iron oxides can be detected from all of the diffraction patterns, indicating that only a single oxide phase is formed in each sample. To further confirm the incorporation of Cu and Fe into the

NiO lattices and determine chemical composition of each sample, EDX spectra are presented in the insets of Figure S2d, S3d, and S4d. At the same time, the EDX quantitative analyses reveal the average atomic ratios of Ni : Cu : O, Ni : Co : O, and Ni : Fe : O are 0.67 : 0.33 : 1, 1 : 2 : 4, and 0.90 : 0.10 : 1, respectively. Thus, these results show that we have synthesized the $Ni_{1-x}Cu_xO$, $NiCo_2O_4$, and $Ni_{1-x}Fe_xO$ NW arrays on CFP.

Note that there are significant discrepancies between the concentration ratio of metallic salts in the initial reaction solution and the corresponding Ni/M atomic ratio in the resultant bimetallic oxide NW precursor. Such discrepancies can be attributed to the differences in the hydrolysis rates between hydrated Ni and M ions under our hydrothermal reaction conditions and different crystal lattice energies of Ni and M in the Ni–M basic carbonate NWs, which lead to the different Ni/M atomic ratio in the Ni–M basic carbonate precursor and thus in the corresponding Ni−M oxide NWs relative to that in the reaction solution. Similarly, the great discrepancies in chemical composition also exist between $NiCo_2O_4$ and $Ni_{1-x}Co_xSe_2$ (see Table 1 in the main text). This can be explained by the lattice reconstruction during the selenization process and different crystal lattice energies of Ni and Co in the Ni−Co oxide and corresponding Ni−Co diselenides, leading to the most stable separate structure. Accordingly, the composition of the resulting $Ni_{1-x}Co_xSe_2$ does not depend on the Ni−Co oxide precursor.

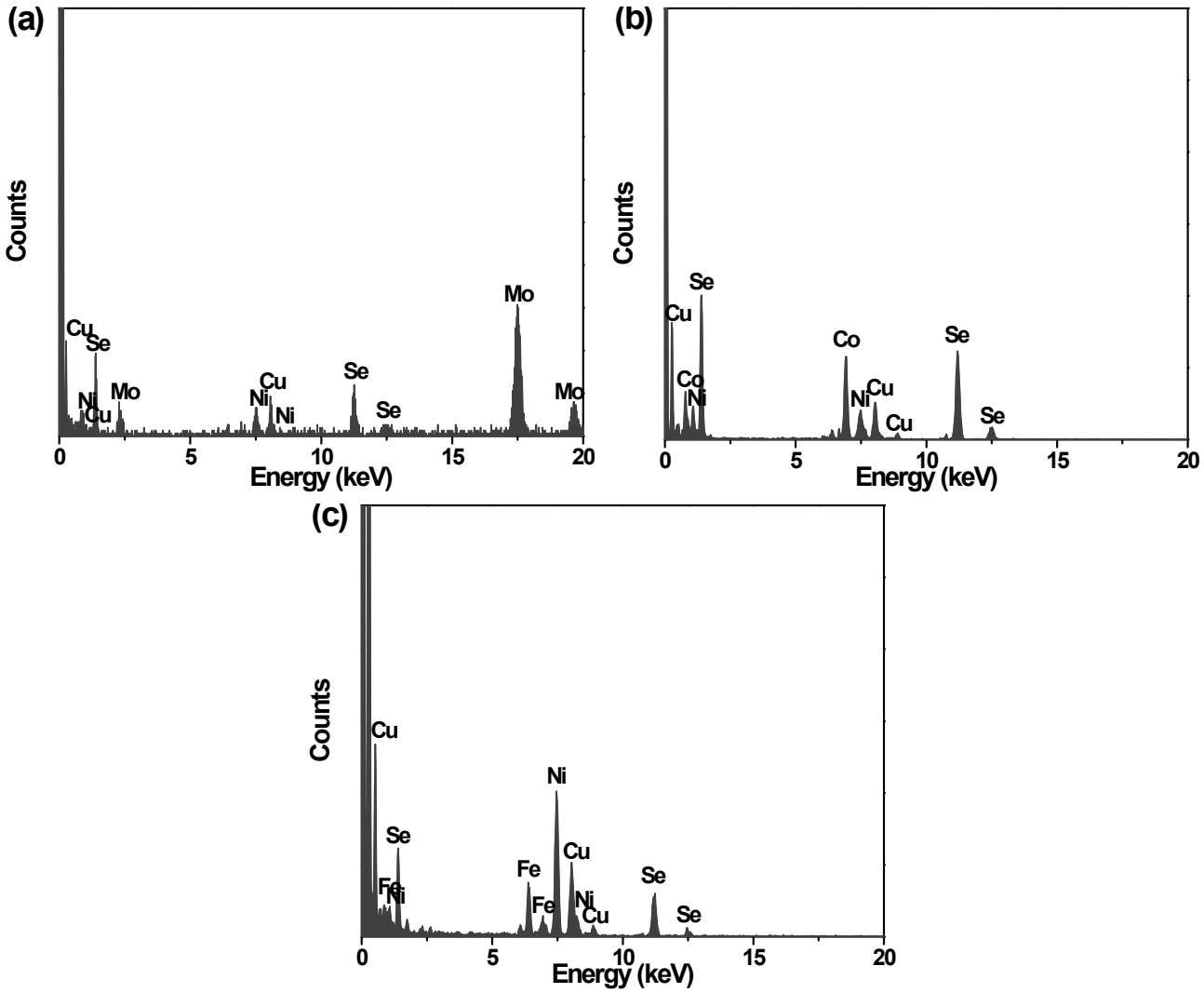

Figure S5. EDX spectra of the as-prepared (a) $Ni_{1-x}Cu_xSe_2$ NWs, (b) $Ni_{1-x}Co_xSe_2$ NWs, and (c) $Ni_{1-x}Fe_xSe_2$ NWs. The Mo signals in panel (a) and Cu signals in panel (b) and (c) stem from the molybdenum and copper grids used for TEM characterization, respectively.

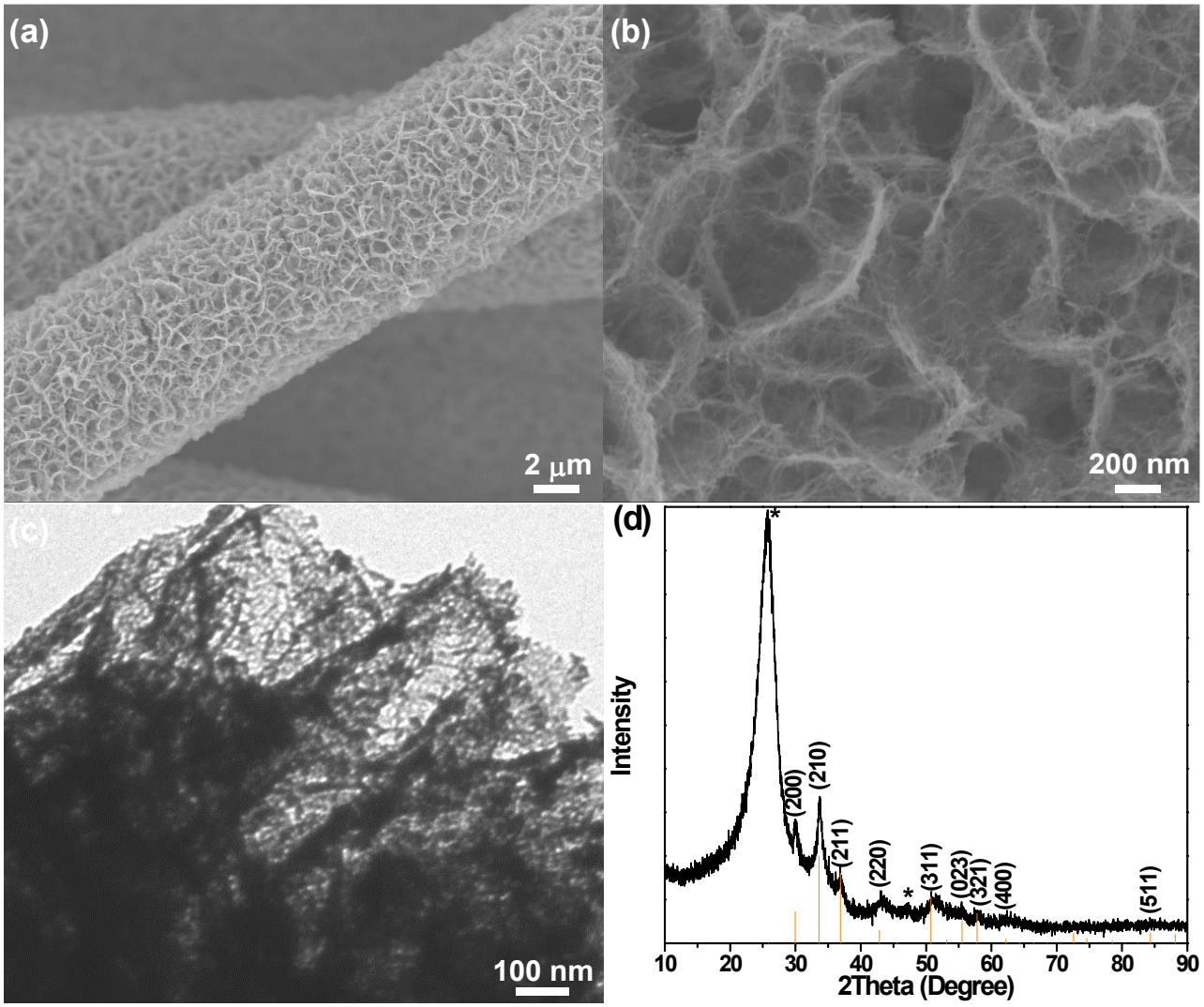

Figure S6. Morphological and structural characterization of the $NiSe_2$/CFP. (a) Low- and (b) high-magnification SEM micrographs, (c) TEM image, and (d) XRD pattern. For comparison, the intensities and positions for the $NiSe_2$ reference are given according to the JCPDS database (JCPDS No. 88-1711, orange lines at the bottom of panel (d)).

The SEM images in Figure S6a and S6b display that the $NiSe_2$ NWs are cross-linked into porous spider web-like networks. The TEM images in Figure S6s exhibits the ultrathin NWs with a diameter of 3–5 nm. The XRD pattern of $NiSe_2$/CFP in Figure S6d shows that the material contains a cubic pyrite phase of $NiSe_2$ besides CFP because all the diffraction peaks from $NiSe_2$ match well with the JCPDS file No. 88-1711.

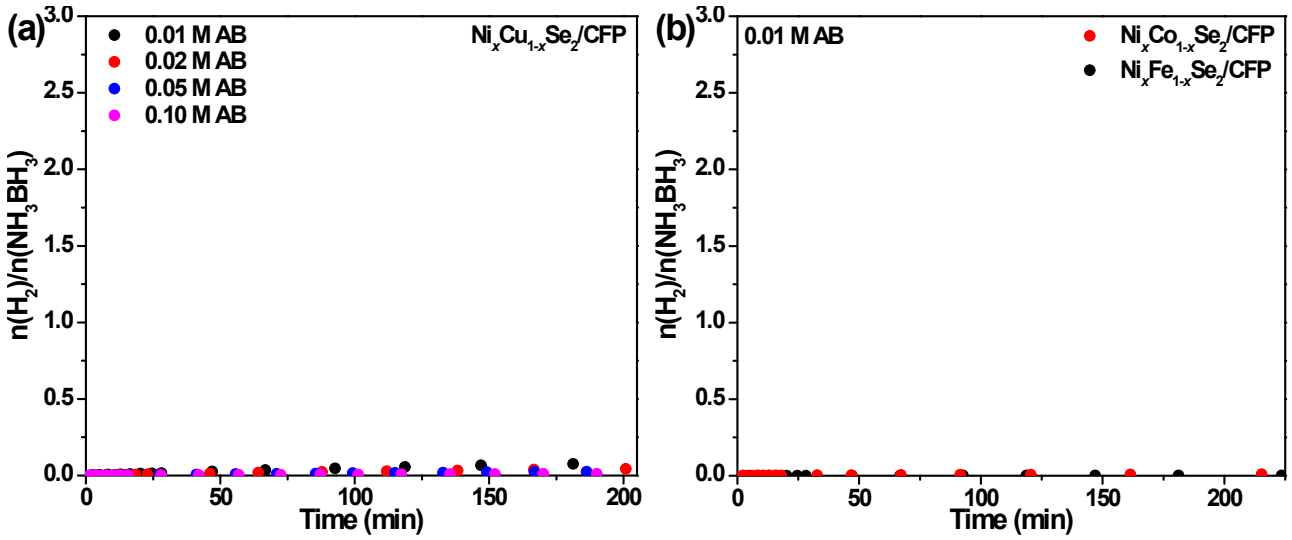

Figure S7. Stoichiometric hydrogen production via the hydrolysis of AB (NH_3BH_3(aq) + $2H_2O$ = NH_4BO_2(aq) + $3H_2$(g)) with the elapse of time in 50 mL of an aqueous solution containing 0.1 M KOH and (a) AB at a different concentration over $Ni_{1-x}Cu_xSe_2$/CFP (1 × 1 cm^2, loading: 2.0 mg cm^{-2}), or (b) 0.01 M AB over different $Ni_{1-x}M_xSe_2$/CFP systems (1 × 1 cm^2, loading: 2.4 and 3.2 mg cm^{-2} for $Ni_{1-x}Co_xSe_2$ and $Ni_{1-x}Fe_xSe_2$, respectively) at room temperature.

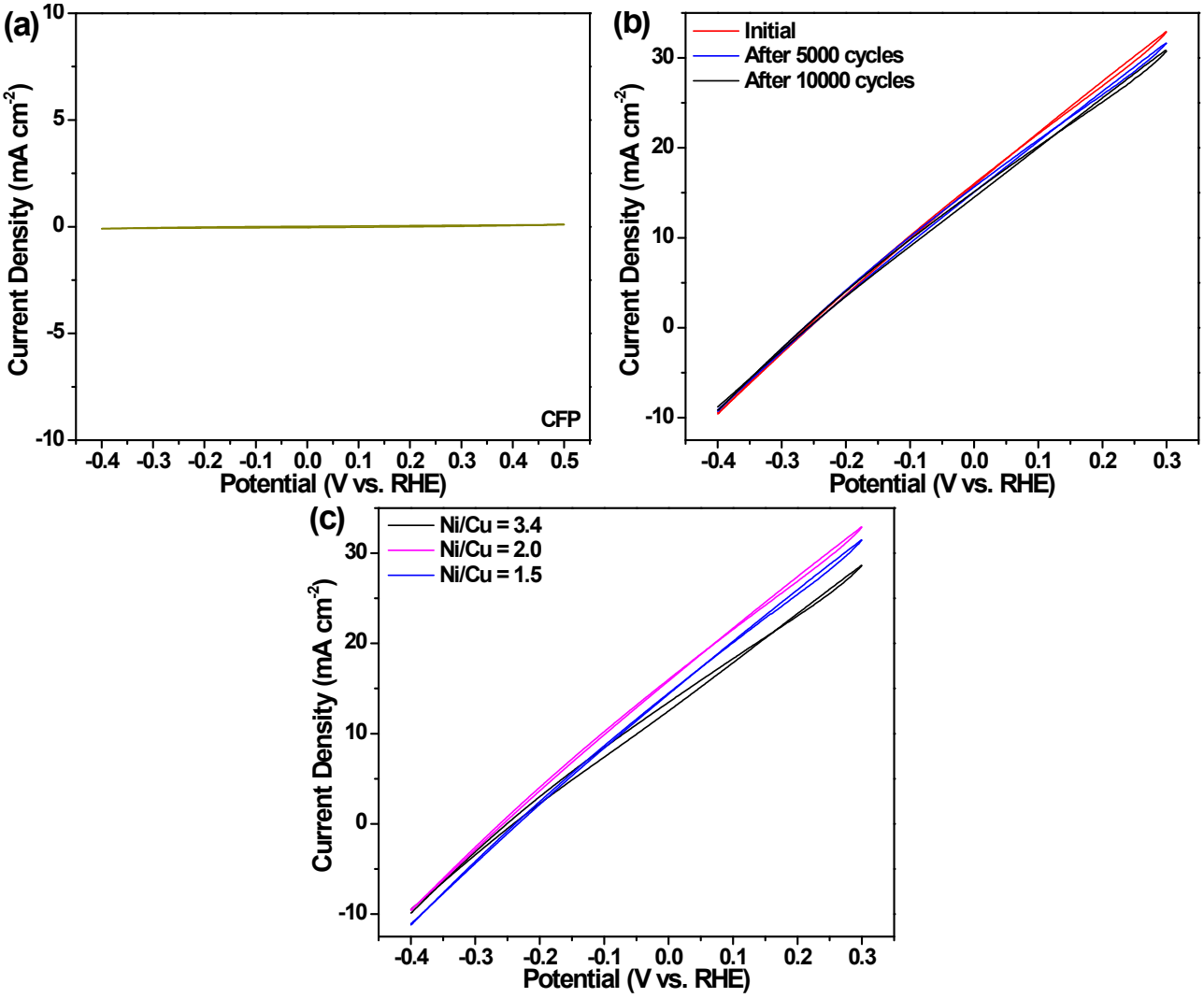

Figure S8. (a) CV measured on the naked CFP in a solution of 0.01 M AB and 0.1 M KOH. (b) CV curves obtained on the $Ni_{1-x}Cu_xSe_2$/CFP anode after 1, 5000, and 10000 potential cycles of the durability test. The sweep rate for the cyclic stability tests was set at 20 mV s^{-1}, during which potential was cycled between –0.4 and 0.3 V vs. RHE. (c) The comparison of CVs obtained from different $Ni_{1-x}Cu_xSe_2$/CFP electrodes with a varied Ni/Cu atomic ratio in a solution of 0.1 M KOH containing 0.1 M AB. The $Ni_{1-x}Cu_xSe_2$/CFP electrodes with a Ni/Cu atomic ratio of 3.4, 2.0, and 1.5 were synthesized with a $NiCl_2/CuCl_2$ molar ratio of 1 : 0.4, 1 : 1.9, or 1 : 2.4, respectively.

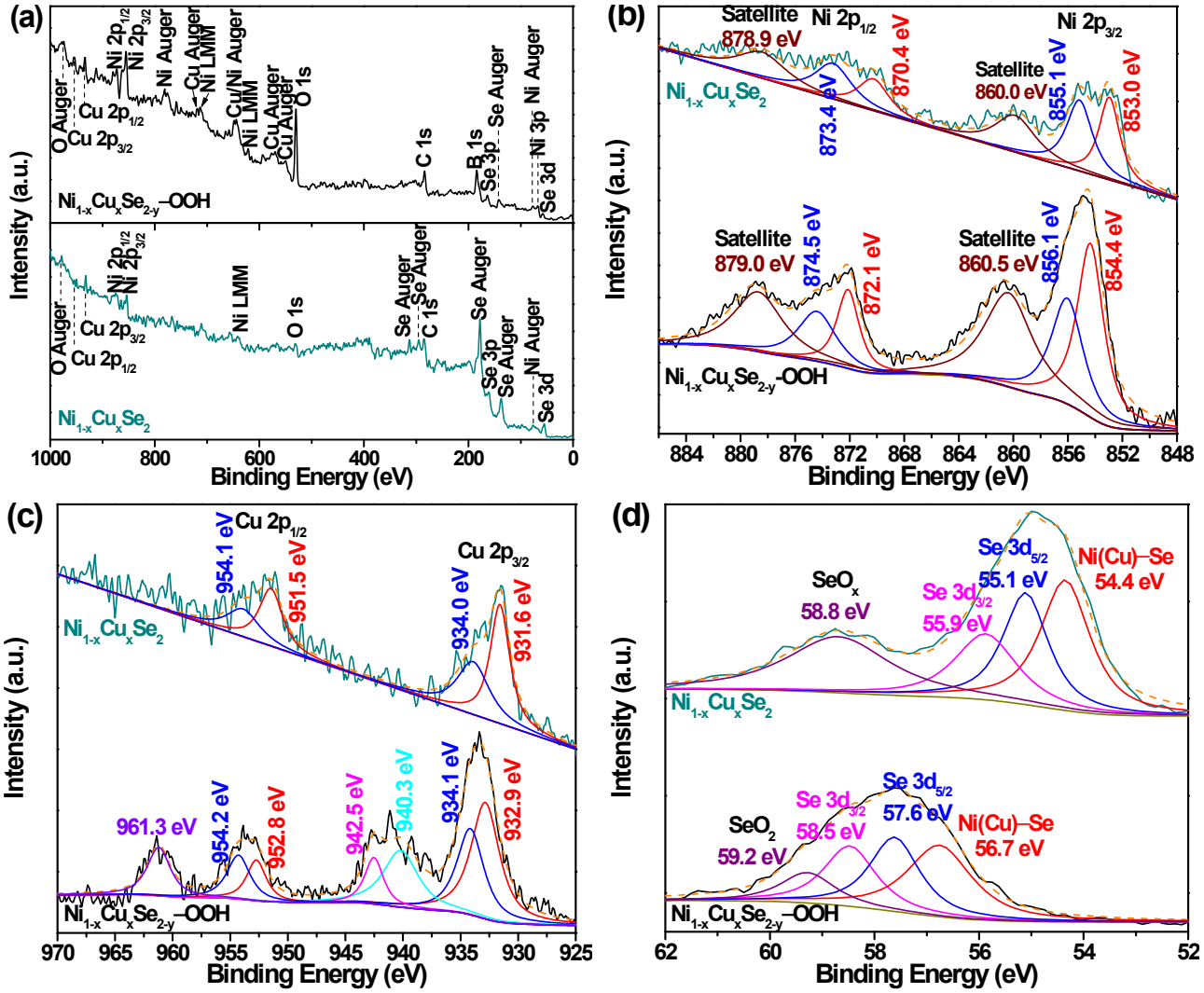

Figure S9. XPS spectra collected from the $Ni_{1-x}Cu_xSe_2$ NWs and $Ni_{1-x}Cu_xSe_{2-y}$–OOH NSs. (a) XPS survey spectrum, (b) Ni 2p, (c) Cu 2p, and (d) Se 3d detail spectra.

The surface chemical compositions and electronic states of the $Ni_{1-x}Cu_xSe_2$ NWs are further analyzed using XPS. The survey spectrum exhibits the presence of Cu, Ni, Se, and O elements (Figure S9a). The surface atomic ratio of Cu : Ni : Se : O is 23.04 : 11.38 : 64.37 : 1.21 for the $Ni_{1-x}Cu_xSe_2$ sample. The Ni 2p core level spectrum can be fitted into two sets of doublets, of which one set consisting of two peaks at 853.0 and 870.4 eV can be readily assigned to the Ni(II) $2p_{3/2}$ and Ni(II) $2p_{1/2}$ signals,[1,2] and the other consisting of two peaks at 855.1 (Ni $2p_{3/2}$) and 873.4 eV (Ni $2p_{1/2}$) corresponds to a Ni(III) component (Figure S9b).[3–5] Concomitantly, two satellite peaks are observed at 860.0 and 878.9 eV in the Ni 2p region, verifying the Ni component in Ni^{2+} and Ni^{3+} valent states. The Cu 2p signals can be fitted into two sets of peaks, one consisting of two peaks centered at 931.6 ($2p_{3/2}$) and 951.5 eV ($2p_{1/2}$), respectively, and the other consisting of two peaks at 934.0 ($2p_{3/2}$) and 954.1 eV ($2p_{1/2}$), respectively (Figure S9c), which can be attributed to the species associated with Cu^+ and Cu^{2+}, respectively.[6,7] In addition, unlike the XPS spectra of the Cu 2p region obtained from most of samples containing Cu species, no characteristic shake-up satellites related to Cu–O or HO···Cu–O species are observed in our $Ni_{1-x}Cu_xSe_2$ NWs, suggesting that the oxide precursor has been completely converted into the selenide. The Se 3d spectrum is fitted into four peaks by deconvolution (Figure S9d). The binding energy (BE) of the main line consisting of a stronger peak at 54.4 eV and a doublet centered at 55.1 ($3d_{5/2}$) and 55.9 ($3d_{3/2}$) arises from the Se species associated with Ni(Cu)−Se and −Se−Se− bonds in $Ni_{1-x}Cu_xSe_2$, respectively.[8,9] At the same time, the BE at 58.8 eV can be assigned to the selenium oxides formed from surface oxidation.[8,9]

For comparison, Figure S9 also shows the XPS spectra of the $Ni_{1-x}Cu_xSe_{2-y}$–OOH sample. The XPS survey spectrum in Figure S9a illustrates an additional B1s signal and a much stronger O 1s peak besides Cu, Ni, and Se elements in the $Ni_{1-x}Cu_xSe_{2-y}$–OOH, demonstrating the appreciable interactions between the $Ni_{1-x}Cu_xSe_{2-y}$–OOH

and AB and/or its oxidized intermediates, such as $BH_3(OH)^-$, $BH_2(OH)_2^-$, $BH(OH)_3^-$, and $B(OH)_4^-$, and the significant superficial oxidation of the $Ni_{1-x}Cu_xSe_{2-y}$−OOH after catalyzing the AOR. This result suggests that AB and/or its oxidized intermediates may serve as the capping agents to control the morphology of NSs. The surface atomic ratio of Ni : Cu : Se : O is 23.04 : 11.54 : 36.72 : 28.70 for the $Ni_{1-x}Cu_xSe_{2-y}$−OOH. The XPS spectrum of the Ni 2p region in Figure S9b shows in addition to a pair of shakeup satellites at 860.5 and 879.0 eV, both sets of the fitted doublets, which are centered at 854.4 and 872.1 eV as well as at 856.1 and 874.5 eV corresponding to the Ni(II) $2p_{3/2}$ and Ni(II) $2p_{1/2}$ as well as the Ni(III) $2p_{3/2}$ and Ni(III) $2p_{1/2}$ signals, respectively, are significantly blue-shifted compared to those of the $Ni_{1-x}Cu_xSe_2$. This feature is unique for the $Ni_{1-x}Cu_xSe_{2-y}$−OOH considering that the Ni(III) $2p_{3/2}$ and Ni(III) $2p_{1/2}$ BEs in $Ni_{1-x}Co_xSe_{2-y}$−OOH (not shown for brevity) and $Ni_{1-x}Fe_xSe_{2-y}$−OOH (see Figure S11 and the related discussions) do not present obvious positive shifts in comparison with the corresponding Ni(III) 2p components in $Ni_{1-x}Co_xSe_2$ and $Ni_{1-x}Fe_xSe_2$. On the other hand, as shown in Figure S9c, the oxidation state of Cu^+ in the $Ni_{1-x}Cu_xSe_{2-y}$−OOH has been boosted, as evidenced by the significant positive shifts of the corresponding peaks to 932.9 and 952.8 eV corresponding to Cu $2p_{3/2}$ and $2p_{1/2}$ of $Cu^{\zeta+}$ ($1 < \zeta < 2$), while the peaks at 934.1 and 954.2 eV retain the same BEs can be ascribed to Cu $2p_{3/2}$ and $2p_{1/2}$ of Cu^{2+}. On the other hand, two extra characteristic shakeup peaks (one fitted into two components with BEs at 940.3 and 942.5 eV and the other with BE at 961.3 eV) related to Cu–O and most likely HO···Cu–O species were also detected on account of surface oxidation and hydroxylation.[6,10] The Se 3d spectrum of the $Ni_{1-x}Cu_xSe_{2-y}$–OOH sample in Figure S9d shows a significant blue-shift relative to that of the $Ni_{1-x}Cu_xSe_2$ NWs due to the surface oxidation by repeatedly running CV for the AOR and can be deconvoluted into four fitted peaks. Compared to the $Ni_{1-x}Cu_xSe_2$ NWs, the corresponding fitted peaks are blue-shifted to 56.7, 57.6, 58.5, and 59.2 eV, respectively.

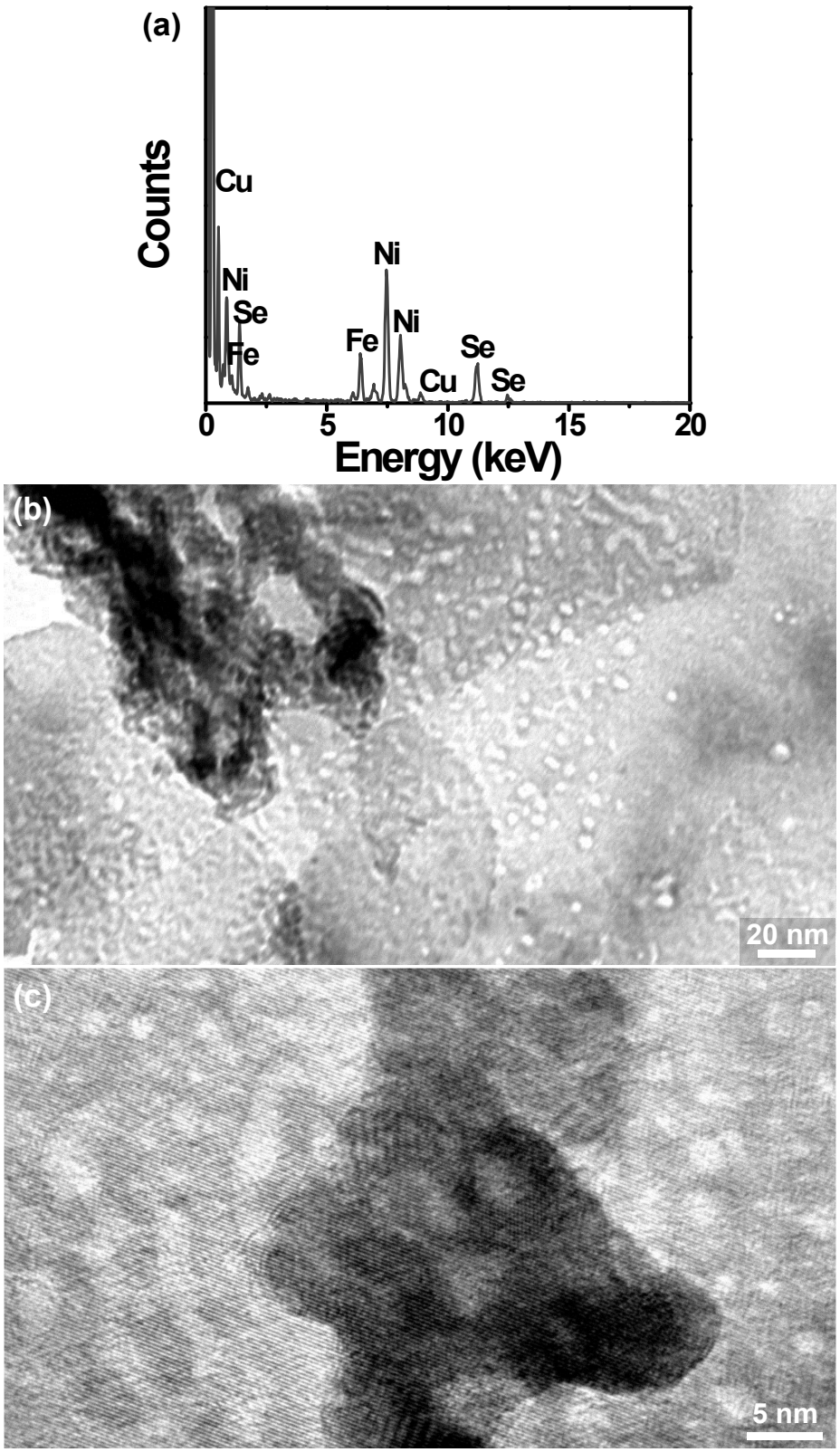

Figure S10. (a) EDS spectrum, (b) low- and (c) high-magnification TEM images of the porous $Ni_{1-x}Fe_xSe_{2-y}$−OOH NSs obtained after the AOR.

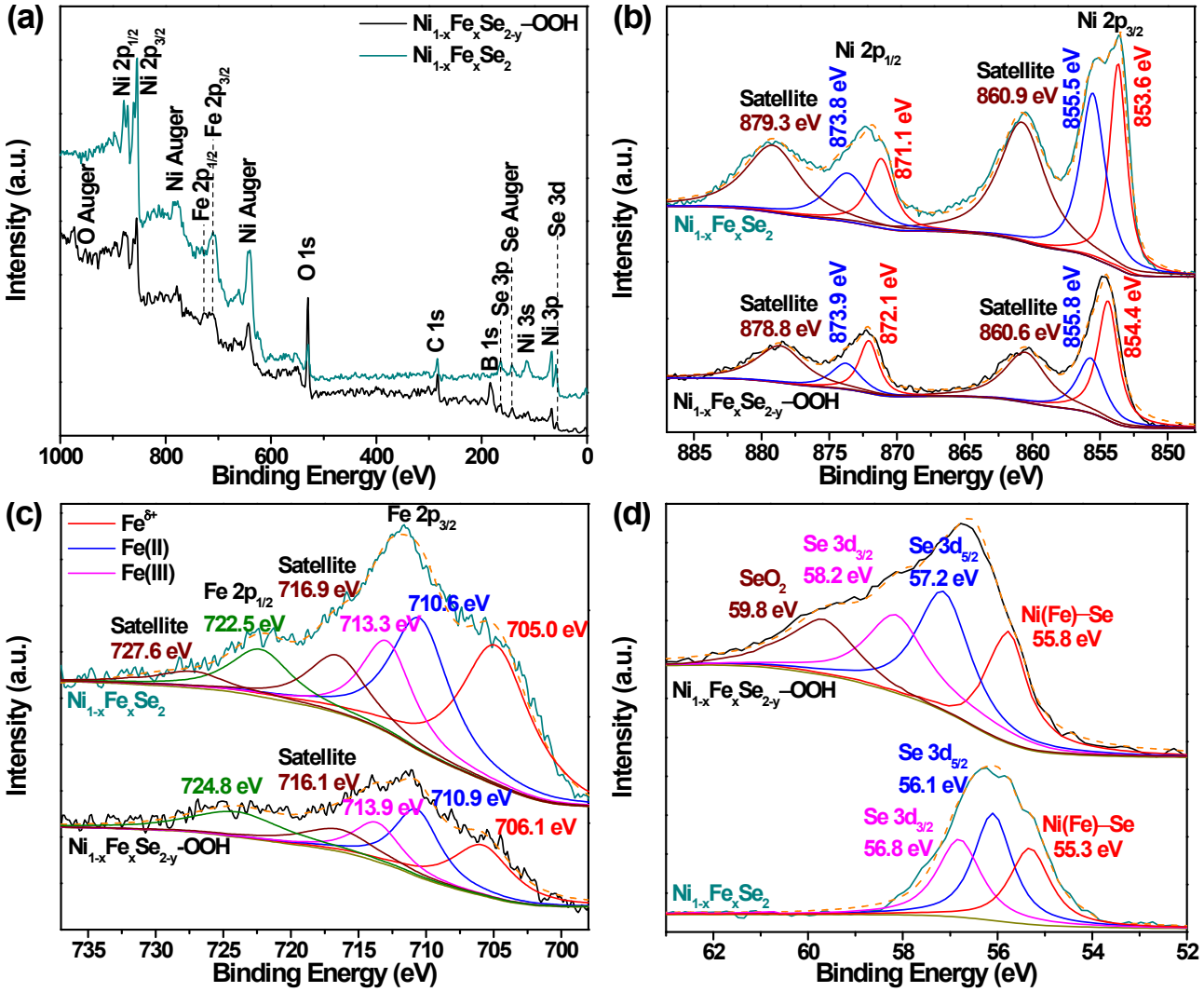

Figure S11. XPS spectra of the $Ni_{1-x}Fe_xSe_{2-y}$–OOH and $Ni_{1-x}Fe_xSe_2$. (a) XPS survey spectra, (b) Ni 2p, (c) Fe 2p, and (d) Se 3d detail spectra.

The XPS survey spectra of the $Ni_{1-x}Fe_xSe_{2-y}$–OOH and $Ni_{1-x}Fe_xSe_2$ in Figure S11a show the Ni, Fe, and Se signals in addition to those from C- and O-containing (surface oxides) species. Note that the B 1s peak appears due to the adsorption of boron-containing species as capping agents on the surface of $Ni_{1-x}Fe_xSe_{2-y}$–OOH NSs after the AOR treatment. The surface atomic ratios of Ni : Fe : Se : O are 21.94 : 9.96 : 35.73 : 32.37 and 24.05 : 8.38 : 63.26 : 4.31 for the $Ni_{1-x}Fe_xSe_{2-y}$–OOH and $Ni_{1-x}Fe_xSe_2$, respectively, based on XPS quantitative analysis, indicating that a significant degree of surface oxidation occurred on the $Ni_{1-x}Fe_xSe_{2-y}$–OOH NSs surface after the AOR-treatment. Figure S11b–d show the Ni 2p, Fe 2p, and Se 3d core-level XPS spectra. In addition to the corresponding shakeup satellite peaks, the fitting analysis of Ni 2p core-level XPS spectra in Figure S11b reveals that the Ni species can be identified as Ni(II) species (853.6 (Ni $2p_{3/2}$) and 871.1 eV (Ni $2p_{1/2}$)) and Ni(III) species (855.5 (Ni $2p_{3/2}$) and 873.8 eV (Ni $2p_{1/2}$)) for the $Ni_{1-x}Fe_xSe_2$,[1–5] and as $Ni^{\varepsilon+}$ ($2 < \varepsilon < 3$) associated with the partially oxidized nickel selenides (854.4 (Ni $2p_{3/2}$) and 872.1 eV (Ni $2p_{1/2}$)) and Ni(III) species (855.8 (Ni $2p_{3/2}$) and 873.9 eV (Ni $2p_{1/2}$)) for the $Ni_{1-x}Fe_xSe_{2-y}$–OOH. In addition, two shakeup satellite peaks at 860.9 and 879.3 eV for the $Ni_{1-x}Fe_xSe_2$ or at 860.6 and 878.8 eV for the $Ni_{1-x}Fe_xSe_{2-y}$–OOH are associated with Ni $2p_{3/2}$ and Ni $2p_{1/2}$, respectively, further demonstrating the Ni in these two samples is in dominant Ni(II) and Ni(III) valent states. In the case of Fe 2p, the peaks at 705.0 and 706.1 eV for the $Ni_{1-x}Fe_xSe_2$ and $Ni_{1-x}Fe_xSe_{2-y}$–OOH, respectively, in the Fe $2p_{3/2}$ region can be ascribed to a partially positive charge Fe species or Fe^0 in the Fe–Se bond ($Fe^{\delta+}$, $0 \le \delta < 2$),[11,12] as shown in Figure S11c. Compared to the $Ni_{1-x}Fe_xSe_2$, both the $Ni^{\varepsilon+}$ 2p and $Fe^{\delta+}$ 2p peaks for the $Ni_{1-x}Fe_xSe_{2-y}$–OOH are dramatically blue-shifted toward the higher BEs, suggesting the higher surface oxidation states of Ni and Fe species on the $Ni_{1-x}Fe_xSe_{2-y}$–OOH NSs after the AOR-treatment due to the electron transfer from positively charged Ni and Fe to the O species (Figure S11c). The blue-shifts of other Fe $2p_{3/2}$ peaks are also appreciable due to the altered Fe

surrounding chemical environment after the formation of Fe−O bond. Such a variation in the electronic structure may also contribute to the difference in catalytic activity between the $Ni_{1-x}Fe_xSe_{2-y}$−OOH and $Ni_{1-x}Fe_xSe_2$. In addition, in the Fe $2p_{3/2}$ region, two extra bands at 710.6 and 713.3 eV for the $Ni_{1-x}Fe_xSe_2$ and 710.9 and 713.9 eV for the $Ni_{1-x}Fe_xSe_{2-y}$−OOH, most likely correspond to the Fe^{2+} and Fe^{3+} arising from FeO_x on the surface, respectively, while the Fe $2p_{1/2}$ peaks are too weak to be given a well-defined fitting (Figure S11c).[13,14] The Fe $2p_{1/2}$ peaks at 722.5 eV for the $Ni_{1-x}Fe_xSe_2$ and 724.8 eV for the $Ni_{1-x}Fe_xSe_{2-y}$−OOH in combination with their related satellite peaks further unveil the Fe oxidation state associated with FeO and Fe_2O_3, according to the data presented by Yamashita et al. (Figure S11c).[15] In the Se 3d region, the peaks at 55.3, 56.1, and 56.8 eV can be attributed to Ni(Fe)−Se bond, Se $3d_{5/2}$ (Se−Se), and Se $3d_{3/2}$ (Se−Se) for the $Ni_{1-x}Fe_xSe_2$, respectively (Figure S11d).[8] In contrast, the Se 3d spectrum of the $Ni_{1-x}Fe_xSe_{2-y}$−OOH shows a new SeO_x peak located at 59.8 eV and the blue shifts of BEs corresponding to Ni(Fe)−Se bond (55.8 eV) and Se−Se bond (Se $3d_{5/2}$ and Se $3d_{3/2}$ peaks centered at 57.2 and 58.2 eV, respectively) as a result of the electron transfer from Se to the O species after surface oxidation of the selenide (Figure S11d).

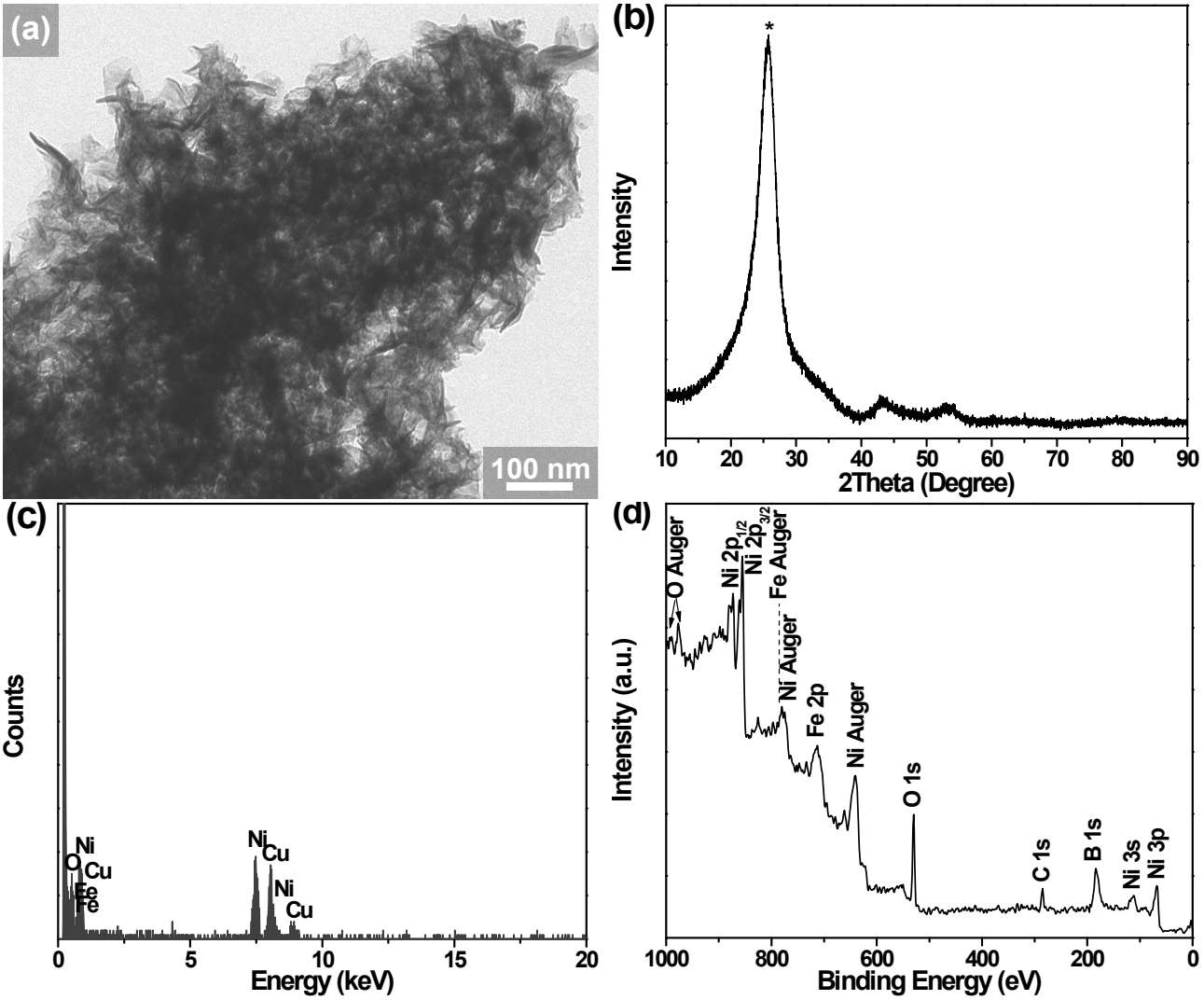

Figure S12. (a) TEM image, (b) XRD pattern, and (c) EDX spectrum of the $Ni_{1-x}Fe_x$-oxyhydroxide NSs converted from $Ni_{1-x}Fe_xSe_2$ NWs after positive-going scan up to 0.3 V vs. RHE for the AOR. These data are independent of the AB concentration reported in this work. No Se signals can be observed from the EDX spectrum and, concomitantly, the O signal appears in panel (c), suggesting that Se atoms have been leached out and the pristine selenide has been converted into hydroxide. (d) XPS survey spectrum of the $Ni_{1-x}Fe_x$-oxyhydroxide NSs.

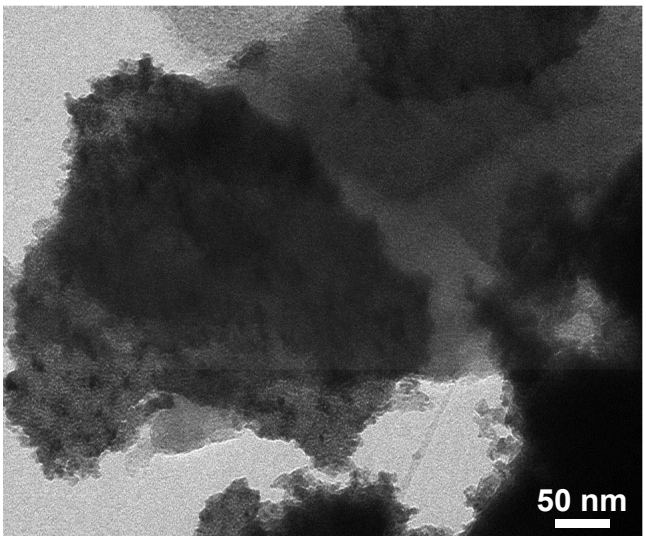

Figure S13. TEM image of the thicker NSs transformed from the $Ni_{1-x}Fe_xSe_2$ NWs, which is obtained in the absence of AB while keeping the other conditions the same as those for performing CV measurements for the AOR.

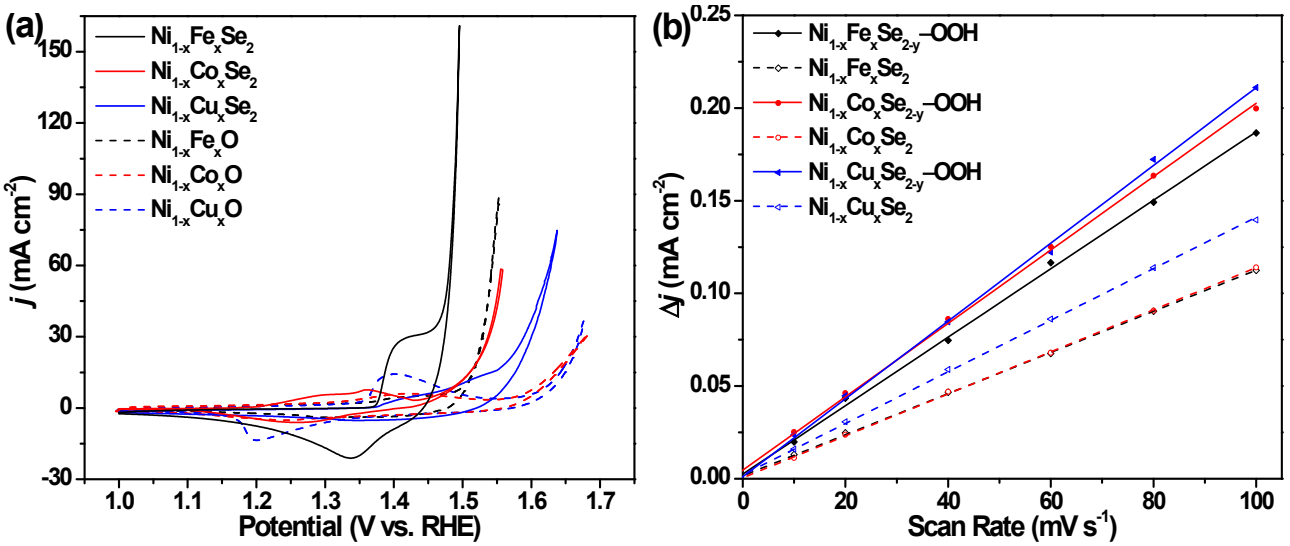

Figure S14. (a) Comparison of the *IR*-corrected CV curves obtained on the $Ni_{1-x}M_xSe_2$/CFP electrodes and the corresponding $Ni_{1-x}M_xO$/CFP precursors for water oxidation in 1 M KOH. Note that the redox peak area of Ni(II)/Ni(III or IV) couple for the $Ni_{1-x}Cu_xO$ NWs is larger than those for the $Ni_{1-x}Co_xO$ and $Ni_{1-x}Fe_xO$ NWs, which can be attributed to the high-density porous structure coupled with the small sizes of the $Ni_{1-x}Cu_xO$ NWs. (b) Plots for the extraction of the double-layer capacitances used for determining the ECSA, which are obtained by $\Delta j = j_a - j_c$ at 0.95 V against scan rate (v).

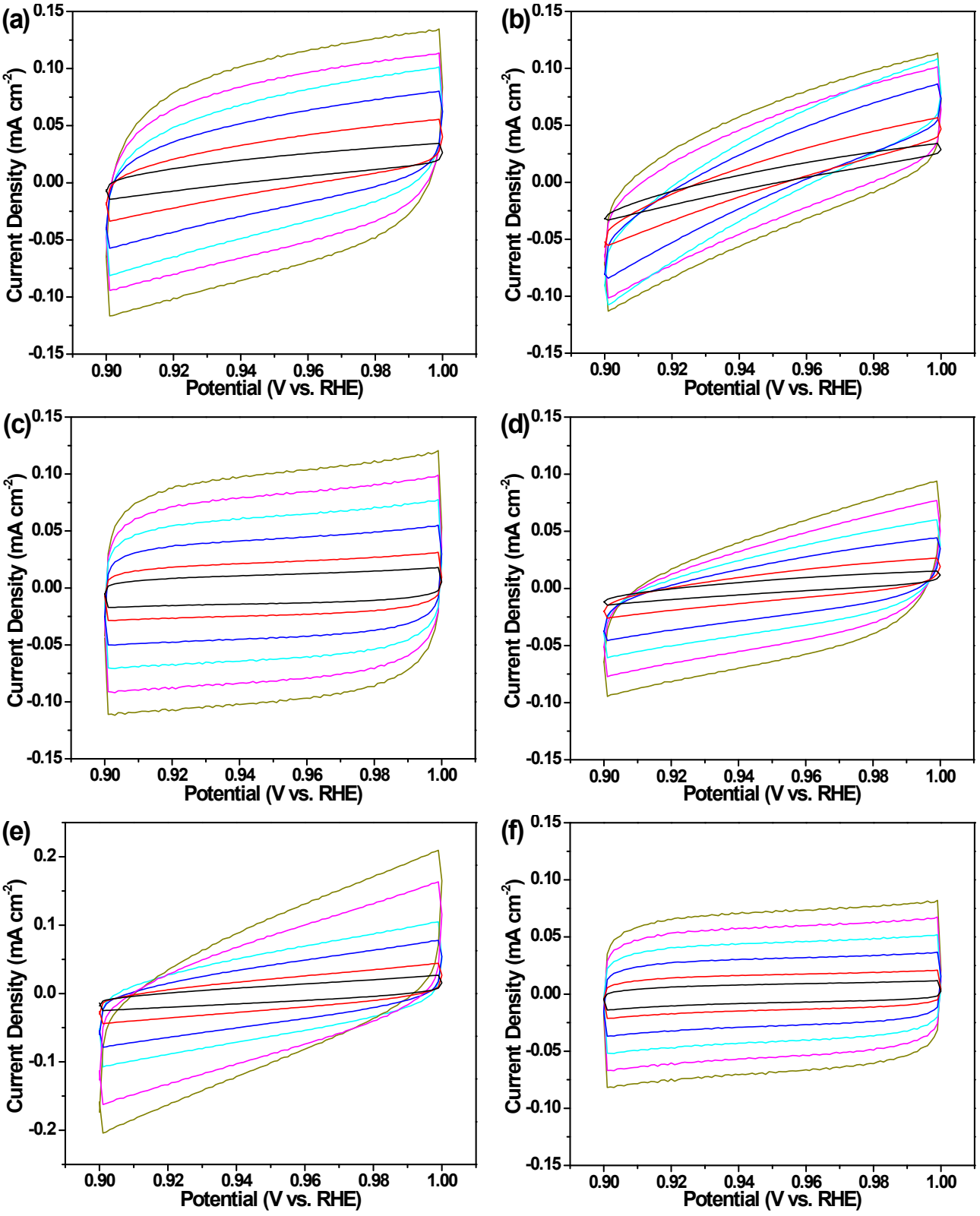

Figure S15. Cyclic voltammograms of the (a) $Ni_{1-x}Fe_xSe_{2-y}(OH)_y$/CFP, (b) $Ni_{1-x}Fe_xSe_2$/CFP, (c) $Ni_{1-x}Co_xSe_{2-y}(OH)_y$/CFP, (d) $Ni_{1-x}Co_xSe_2$/CFP, (e) $Ni_{1-x}Cu_xSe_{2-y}(OH)_y$/CFP, and (f) $Ni_{1-x}Cu_xSe_2$/CFP electrodes, which are used to estimate the double layer capacitances (C_{dl}). Sweep rates at 10, 20, 40, 60, 80 and 100 mV s^{-1} were chosen.

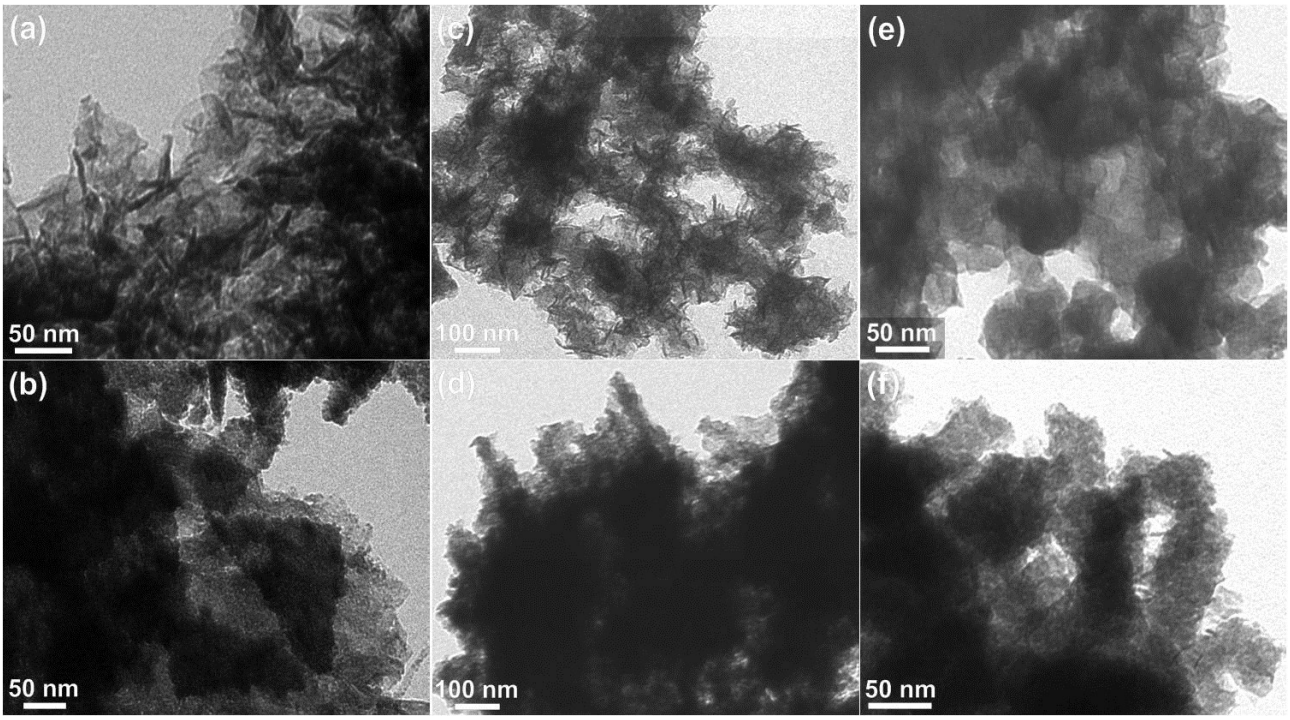

Figure S16. Morphological characterization of $Ni_{1-x}M_xSe_{2-y}$−OOH and $Ni_{1-x}M_xSe_2$ obtained after the OER. TEM images of (a) $Ni_{1-x}Fe_xSe_{2-y}$−OOH, (b) $Ni_{1-x}Fe_xSe_2$, (c) $Ni_{1-x}Co_xSe_{2-y}$−OOH, (d) $Ni_{1-x}Co_xSe_2$, (e) $Ni_{1-x}Cu_xSe_{2-y}$−OOH, and (f) $Ni_{1-x}Cu_xSe_2$.

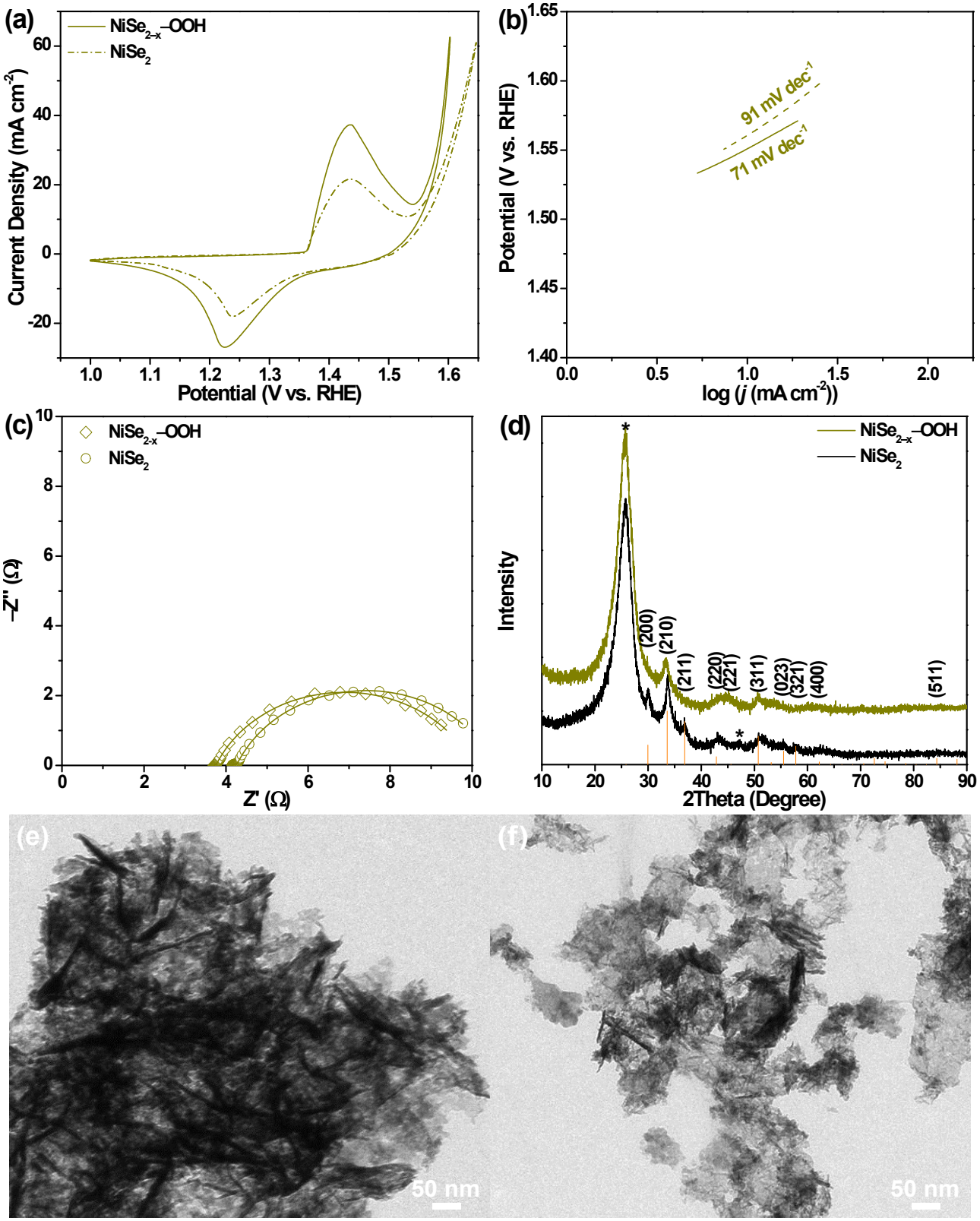

Figure S17. Electrocatalytic performance of $NiSe_{2-x}$–OOH/CFP and $NiSe_2$/CFP electrodes for water oxidation in 1 M KOH. (a) Comparison of the *IR*-corrected CV curves. (b) Polarization curves-derived Tafel slopes. (c) EIS Nyquist plots. (d) XRD patterns. TEM images of (e) $NiSe_2$ and (f) $NiSe_{2-x}$–OOH.

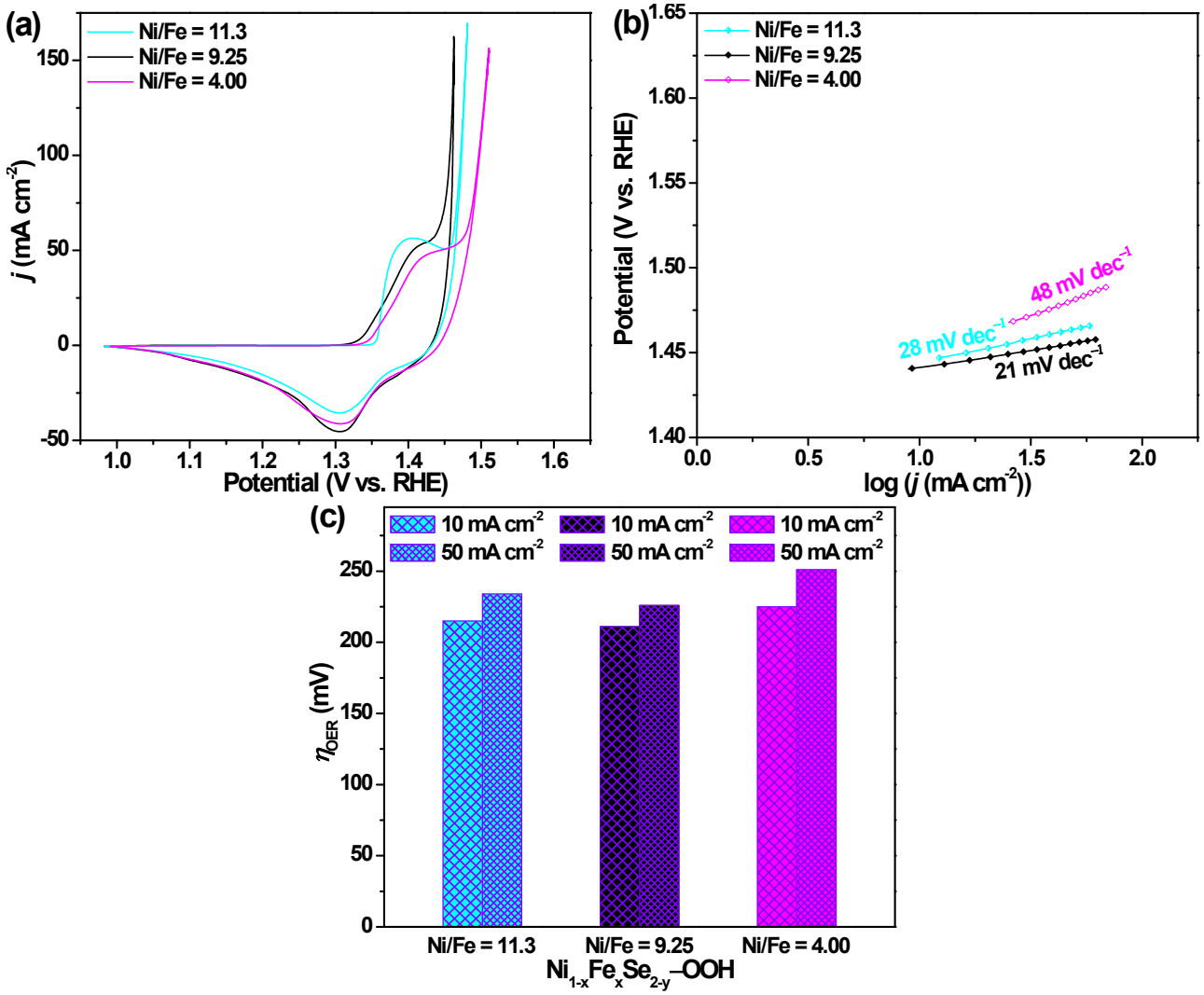

Figure S18. (a) The *IR*-corrected CV curves, (b) polarization curves-derived Tafel slopes, and (c) comparison of η_{OER} at j = 10 and 50 mA cm^{-2} of various $Ni_{1-x}Fe_xSe_{2-y}$–OOH/CFP with a different Ni/Fe ratio in 1 M O_2-saturated KOH. The $Ni_{1-x}Fe_xSe_{2-y}$–OOH/CFP with a Ni/Fe atomic ratio of 9.25, 11.3, or 4.00 was synthesized with a $NiCl_2/FeCl_3$ molar ratio of 2 : 1, 3 : 1, or 1 : 1, respectively, and then underwent the same AOR-treatment.

Table S1. Comparison of electrocatalytic activities of the $Ni_{1-x}Cu_xSe$/CFP anode and other electrodes reported in the literature for AOR.

Catalysts	Onset potential (V vs. RHE)	Oxidation current [a] (mA cm^{-2})	Catalyst loading (mg cm^{-2})	Electrolyte solution	scan rate (mV s^{-1})	Ref in the text
Ag(30 wt%)/C	−0.104	~20 (0.446 V)	not mentioned	0.1 M AB + 2 M KOH	5	8
Au disk	not mentioned	~11 (0.646 V)	not mentioned	0.01 M AB + 2 M NaOH	100	31
NPG wire array	−0.230	13.1 (0.570 V)	not mentioned	0.02 M AB + 1 M NaOH	10	32
Fe@Pt NPs/C	ca. −0.090[b]	6.0 (0.370 V)[b] 7.5 (0.870 V)[b]	0.0246 for Pt	0.01 M AB + 1 M NaOH	10	29
Pt/C	ca. −0.060[c]	30 (0.669 V)[c]	0.5 for Pt	0.01 M AB + 1 M NaOH	25	30
Pd/C	ca. −0.275[c]	30 (0.641 V)[c]	0.5 for Pd	0.01 M AB + 1 M NaOH	25	30
Ni_3Co/C	−0.090[b]	5 (0.3 V)[b]	0.255 for Ni_3Co	5 mM AB + 0.1 M NaOH	10	33
Ni_3Pd/C	−0.030[b]	10 (0.5 V)[b]	0.255 for Ni_3Pd	5 mM AB + 0.1 M NaOH	10	33
Ni_3Ag/C	−0.050[b]	6.3 (0.5 V)[b]	0.255 for Ni_3Ag	5 mM AB + 0.1 M NaOH	10	33
$Ni_{1-x}Cu_xSe_2$/CFP	−0.117	4.91 (0.3 V)	2.0	5 mM AB + 0.1 M KOH	10	This work
$Ni_{1-x}Cu_xSe_2$/CFP	−0.148	7.05 (0.3 V)	2.0	0.01 M AB + 0.1 M KOH	10	This work
$Ni_{1-x}Cu_xSe_2$/CFP	−0.182	11.31 (0.3 V)	2.0	0.02 M AB + 0.1 M KOH	10	This work
$Ni_{1-x}Cu_xSe_2$/CFP	−0.256	32.9 (0.3 V)	2.0	0.1 M AB + 0.1 M KOH	10	This work

[a] The potential value corresponds to the oxidation current density and is expressed on the RHE scale. [b] The values are obtained on the electrode at a rotation rate of 1600 rpm. [c] The values are obtained on the electrode at a rotation rate of 1000 rpm.

Table S2. Comparison of the electrocatalytic activity of various Ni-based bimetallic catalysts in the literature with $Ni_{1-x}MSe_{2-y}$−OOH/CFP in this work for the OER

Catalysts	η_{OER} (mV) at j (mA cm^{-2})	Tafel slope (mV dec^{-1})	Ref
$(Ni, Co)_{0.85}Se$ NTs	255 at 10	79	*Adv. Mater.*, 2016, **28**, 77−85
$NiCo_2Se_4$ holey NSs	290 at 10	53	*ACS Nano*, 2017, **11**, 9550−9557
$Co_{0.13}Ni_{0.87}Se_2$/Ti	320 at 100	63	*Nanoscale*, 2016, **8**, 3911–3915
$NiCo_2S_4$ NW/NF	260 at 10	40.1	*Adv. Funct. Mater.*, 2016, **26**, 4661−4672
NiCoP-NP/NF	280 at 10	87	*Nano Lett.*, 2016, **16**, 7718−7725
NiCoP/rGO	270 at 10	65.7	*Adv. Funct. Mater.*, 2016, **26**, 6785−6796
Co4Ni1P NTs	245 at 10	61	*Adv. Funct. Mater.*, 2017, **27**, 1703455
CoNi(20 : 1)-P-NS/NF	209 at 10	52	*Energy Environ. Sci.*, 2017, **10**, 893−899
PPy/FeTCPP/Co	340 at 10	61	*Adv. Funct. Mater.*, 2017, **27**, 1606497
NiO/CoN PINWs	300 at 10	30	*ACS Nano*, 2017, **11**, 2275−2283
NiS_2/CoS_2–O NWs	235 at 10	31	*Adv. Mater.*, 2017, **29**, 1704681
Ni–Co–S/NF	270 at 40	133.8	*J. Mater. Chem. A*, 2018, **6**, 12506−12514
$Ni_{1-x}Co_xSe_{2-y}$−OOH/CFP	233 at 10	56	in this work
NiFe/NF	215 at 10	28	*Nature Commun.*, 2015, **6**, 6616
$Co_{0.85}Se$/NiFe-LDH	270 at 150	57	*Energy Environ. Sci.*, 2016, **9**, 478−483
NiCoFe LTHs/CFC	239 at 10	32	*ACS Energy Lett.*, 2016, **1**, 445−453
$Ni_xFe_{1-x}Se_2$ NPs	195 at 10	28	*Nature Commun.*, 2016, **7**, 12324
Ni-Fe-Se cages	240 at 10	24	*Adv. Mater.*, 2017, **29**, 1703870

$(Ni_{0.75}Fe_{0.25})Se_2$ NSs/CFC	255 at 35	47.2	*ACS Appl. Mater. Interfaces*, 2016, **8**, 19386−19392
$Ni_{0.76}Fe_{0.24}Se$/NF	197 at 10	56	*Nano Res*., 2018, **11**, 2149−2158
Ni(Fe)S_2@Ni(Fe)OOH	230 at 10	42.6	*J. Mater. Chem. A*, 2017, **5**, 4335−4342
NiFeS-2 NPs	286 at 10	56.3	*Small*, 2017, **13**, 1700610
FeNiP-NP/NF	180 at 10	76	*Adv. Mater*., 2017, **29**, 1704075
$(Fe_{0.5}Ni_{0.5})_2P$-NSs/NF	156 at 10	66	*Nano Energy*, 2017, **38**, 553−560
a-NiFe-OH/NiFeP/NF	199 at 10	39	*ACS Energy Lett*., 2017, **2**, 1035−1042
NiFeSP-NSs/NF	240 at 50	76.3	*ACS Nano*, 2017, **11**, 10303−10312
Ni_3FeN/Co,N-CNF	270 at 10	51	*Nano Energy*, 2017, **40**, 382−389
Ni_5P_4/NiP_2/NiFe-LDH	197 at 10	46.6	*J. Mater. Chem. A*, 2018, **6**, 13619–13623
$Ni_{1-x}Fe_xSe_{2-y}$−OOH/CFP	211 at 10	21	In this work
$Ni_{1-x}Fe_xSe_{2-y}$−OOH/CFP	266 at 50	21	In this work

References

1. A. W. Peters, Z. Li, O. K. Farha and J. T. Hupp, *ACS Appl. Mater. Interfaces*, 2016, **8**, 20675−20681.
2. X. Yan, L. Tian and X. Chen, *J. Power Sources*, 2015, **300**, 336−343.
3. A. Sivanantham, P. Ganesan and S. Shanmugam, *Adv. Funct. Mater*., 2016, **26**, 4661−4672.
4. D. Friebel, M. W. Louie, M. Bajdich, K. E. Sanwald, Y. Cai, A. M. Wise, M.-J. Cheng, D. Sokaras, T.-C. Weng and R. Alonso-Mori, *J. Am. Chem. Soc*., 2015, **137**, 1305−1313.
5. Z. Wang, J. Li, X. Tian, X. Wang, Y. Yu, K. A. Owusu, L. He and L. Mai, *ACS Appl. Mater. Interfaces*, 2016, **8**, 19386−19392.
6. C. D. Wagner, W. M. Riggs, L. E. Moulder and G. E. Muilenberg, *Handbook of X-ray Photoelectron spectroscopy*, Perkin-Elmer Corporation Physical Electronics Division, U.S.A., 1979.
7. M. Yin, C.-K. Wu, Y. Lou, C. Burda, J. T. Koberstein, Y. Zhu and S. O'Brien, *J. Am. Chem. Soc*., 2005, **127**, 9506−9511.
8. J. Nai, Y. Lu, L. Yu, X. Wang and X. W. Lou, *Adv. Mater*., 2017, **29**, 1703870.
9. T. Chen and Y. Tan, *Nano Res*., 2018, **11**, 1331−1344.
10. Q. Yu, X. Ma, Z. Lan, M. Wang and C. Yu, *J. Phys. Chem. C*, 2009, **113**, 6969−6975.
11. C. Powell, *J. Electron Spectrosc. Relat. Phenom*., 2012, **185**, 1−3.
12. L. Wu, T. Wu, M. Mao, M. Zhang and T. Wang, *Electrochim. Acta*, 2016, **194**, 357−366.
13. B. Zhang, H. Ni, R. Chen, W. Zhan, C. Zhang, R. Lei and Y. Zha, *Appl. Surf. Sci*., 2015, **351**, 1161−1168.
14. B. Zhang, Y. H. Lui, H. Ni and S. Hu, *Nano Energy*, 2017, **38**, 553−560.
15. T. Yamashita and P. Hayes, *Appl. Surf. Sci*., 2008, **254**, 2441.